

Task-specific multispectral band selection

Sebastian J. Wirkert ^{a,*}, Fabian Isensee ^{b,f,*}, Anant S. Vemuri ^a, Leonardo A. Ayala ^a, Klaus H. Maier-Hein ^b, Baowei Fei ^{c,d,e}, and Lena Maier-Hein ^a

^aDivision of Computer Assisted Medical Interventions (CAMI), German Cancer Research Center (DKFZ), Heidelberg, Germany

^bDivision of Medical Image Computing (MIC), German Cancer Research Center (DKFZ), Heidelberg, Germany

^cDepartment of Bioengineering, The University of Texas at Dallas, Richardson, Texas, United States

^dAdvanced Imaging Research Center, The University of Texas Southwestern Medical Center, Dallas, Texas, United States

^eDepartment of Radiology, The University of Texas Southwestern Medical Center, Dallas, Texas, United States

^fFaculty of Biosciences, University of Heidelberg, Heidelberg, Germany

*Authors contributed equally

ABSTRACT

Multispectral imaging provides valuable information on tissue composition such as hemoglobin oxygen saturation. However, the real-time application of this technique in interventional medicine can be challenging because the acquisition time of large amount of hyperspectral data with hundreds of bands can be long. This challenge can partially be addressed by choosing a discriminative subset of bands. The band selection methods proposed to date are mainly based on the availability of often hard to obtain reference measurements. We address this bottleneck with a new approach to band selection that leverages highly accurate Monte Carlo simulations. We hypothesize that a so chosen small subset of bands can reproduce or even improve upon the results of a quasi continuous spectral measurement. We further investigate whether novel domain adaptation techniques can address the inevitable domain shift stemming from the use of simulations. Initial results based on *in silico* and *in vivo* experiments suggest that 10-20 bands are sufficient to closely reproduce results from 101 band spectral measurement in the 500-700nm range, depending on the experiment. The investigated domain adaptation technique, which only requires unannotated *in vivo* measurements yielded better results than the pure *in silico* band selection method. Overall, our method could guide development of novel and fast multispectral imaging systems suited for interventional use without relying on complex hardware setups or manually labeled data.

Keywords: Multispectral, hyperspectral, Monte Carlo, blood oxygenation, machine learning, domain adaptation, feature selection

1. INTRODUCTION

Multispectral imaging (MSI) could be useful for many applications in surgery, including tumor detection and perfusion monitoring.¹ Acquisition of many spectral bands, however, leads to long imaging times and/or low resolution, hampering widespread adoption of the technique. To overcome this issue, current research focuses on reducing the number of recorded bands. Yet, the methods proposed are not able to consider both the target domain (e.g. liver surgery) and the specific task (e.g. oxygenation or blood volume fraction monitoring) when selecting bands.

Please address your correspondence to Lena Maier-Hein, e-mail: l.maier-hein@dkfz-heidelberg.de

Table 1: Overview on relevant band selection methods.

Group	Modality	label-free	Method	Data	Application
Wood et al. ¹¹	Fluorescence	no	wrapper	<i>ex vivo</i>	cancer detection
Han et al. ¹²	MSI	no	filter	<i>in vivo</i>	cancer detection
Nouri et al. ^{13,14}	MSI	yes	filter	<i>in vivo</i>	visualization
Gu et al. ¹⁵	MSI	yes	filter	<i>in vivo</i>	abnormalities
Wirkert et al. ¹⁶	MSI	yes	filter	<i>in vivo</i>	physiological parameters
Marois et al. ¹⁷	MSI	yes	wrapper	<i>in silico</i>	physiological parameters
Preece et al. ¹⁸	MSI	yes	wrapper	<i>in silico</i>	physiological parameters
Proposed	MSI	yes	wrapper	<i>in vivo</i>	physiological parameters

In this paper, we investigate a method that can provide task-specific and target domain-specific band selection. The generic applicability of our approach is achieved with highly generic Monte Carlo-based tissue simulations that aim to capture a large range of optical tissue parameters potentially observed during surgical interventions. The adaptation of the model to a specific clinical application is based on label-free *in vivo* hyperspectral recordings using a recently published approach to multispectral domain adaptation. The bands are selected based on their performance to estimate a task-dependent physiological parameter.

This manuscript is organized as follows: Section 2 gives a detailed overview on the current state of the art. Section 3 describes the method outlined above in more detail. In Section 4 we validate the method *in silico* and with *in vivo* data from.² The manuscript closes with a discussion of the findings in Section 5.

2. STATE OF THE ART IN MULTISPECTRAL BAND SELECTION

A large body of work in band selection is available in the field of remote sensing (see e.g.³⁻⁷). Moreover, band selection is employed in fields like food safety⁸ and histopathology.⁹ This state of the art review will be restricted to algorithms related to interventional imaging, as summarized in Table 1.

Band selection is closely linked to variable/feature selection, in which algorithms can be grouped roughly in filter, wrapper and embedded methods.¹⁰ Filter methods determine the best features as an independent preprocessing step. Wrapper methods use the downstream processing pipeline as a black box and optimize feature sets using this pipeline to maximize its target performance metric for a given task (e.g. accuracy of tumor detection). Finally, embedded methods are directly part of the training process of a machine learning algorithm trying to find a solution to a specific task. While filter methods can rely on unsupervised correlation analysis, wrapper and embedded methods usually need labelled training data. Band selection is different from dimensionality reduction methods such as principal component analysis (PCA), which reduce the dimensionality by finding a subset composed of combinations of bands/features. This does not reduce imaging time, because usually all bands have to be recorded to compute the axes found by PCA.

The following paragraphs briefly review the relevant state of the art approaches with a focus on method, application and results:

Wood et al.¹¹ explored band selection in context of distinguishing fluorophores. They selected the bands which maximize the Area Under the Curve (AUC) of a Naïve Bayesian classifier’s Receiver Operating Characteristic (ROC). More specifically they used a greedy algorithm to remove bands which contribute the least to the AUC while having a low AUC if taken on their own. The algorithm was evaluated on phantoms and lung cancer biopsies, which were stained with an exogenous fluorophore. The authors concluded that three wavelengths provide essentially as much information as using all sixteen wavelengths.

Han et al.¹² selected the most discriminative bands for detecting gastric tumors. These were selected by maximizing the symmetric class-conditional Kullback-Leibler (KL) divergence. A sub-optimal, greedy search algorithm⁸ was chosen because the number of subsets grows exponentially with the number of bands. This algorithm iteratively adds bands to the selection set based on the largest incremental increase on the symmetric KL measure. After selecting the bands in this manner, an SVM was trained to detect cancerous tissue on a pixel level. The algorithm was evaluated on 12 patients and a total of 21 colorectal tumors and bands recorded in the visible wavelength range. The authors concluded that reasonable tumor detection performance can be achieved with 5 out of 28 bands.

Nouri et al.^{13,14} inspected a number of unsupervised, thus label-free, band selection algorithms. The algorithms, originating from the remote sensing community, were evaluated within the context of hyperspectral ureter surgery. Compared to other state-of-the-art works, the band selection was performed in a large spectral range (400-1700nm), enabled by using a system consisting of two cameras, one for the visible to near infrared and one for the near to short-wavelength infrared spectral range. Instead of finding bands which separate a certain class, the authors aimed to find three bands for better visualization (instead of RGB) to present to the surgeon. They evaluated the differing methods by several contrast and entropy measures and measured how the bands can differentiate structures such as the ureter and fat. They found that the three best wavelengths to discriminate ureter tissue are situated in the near infrared and that the Sheffield Index preserves a maximum of information. An interesting additional finding is the fact that inclusion of mid-infrared information provides substantially better discrimination results. Unfortunately incorporating middle infrared bands is not possible for silicon based standard cameras, as the material is not sensitive to light in this range.

Gu et al.¹⁵ selected three bands to discriminate gastric abnormalities from benign tissue. As^{13,14} they aimed to replace the RGB image with the selected bands. Their algorithm first selected the band with the highest variance from a set of 27 bands in the visible range. Subsequent bands were added iteratively with the criterion of minimizing mutual information compared to the previous selection. The bands were determined using 29 images from 12 patients with gastric abnormalities. The authors claim that the selected bands increase contrast.

Wirkert et al.¹⁶ selected bands in a completely unsupervised manner by maximizing the differential entropy contained in the selected subset of bands. More specifically they selected the subset of bands with the highest determinant of the bands' covariance matrix. Under the assumption of an underlying normal distribution this determinant is proportional to differential entropy and thus information contained in the band combination. They tested the method in an *in vivo* porcine setting and concluded that a selection of eight bands leads to oxygenation values close to the 20 bands baseline.

Marois et al.¹⁷ selected bands by analyzing the absorption matrix, assuming oxygenation can be computed from the modified Beer-Lambert's law and leveraging a wavelength dependent path length factor. They chose bands that maximize the product of the singular values of the absorption matrix, arguing this maximizes the orthogonality of the fitted spectra. They evaluated the quality of the chosen bands in an *in silico* setting in the visible and infrared and report the root mean squared error of estimated concentrations of water, oxygenated- and deoxygenated hemoglobin. The three most wavelengths reported by their algorithm are 578, 604 and 975nm.

Preece et al.¹⁸ selected bands with a different idea. First Kubelka-Munk light transport theory based simulations were created for assessing pigmentation of human skin. After adapting these simulations to a set of virtual filters, a genetic algorithm was employed to find the best subset for recovering papillary dermis thickness and blood/melanin content. They ensured the bands can invert the parameters uniquely by differential-geometric reasoning. Incorporation of ground truth from simulations allowed circumventing problems related to references from real data as mentioned in.² The authors concluded that three bands selected according to their method lead to better results than RGB, but RGB leads to reasonable results in the investigated context.

Table 2: The simulated ranges of physiological parameters, and their usage in the simulation set-up.

	$v_{\text{hb}}[\%]$	$s[\%]$	$a_{\text{mie}}[\frac{1}{\text{cm}}]$	b_{mie}	g	n	$d[\text{mm}]$
layer 1-3:	0-30	0-100	5-50	.3-3	.8-.95	1.33-1.54	.02-2
$\mu_a(v_{\text{hb}}, s, \lambda) = v_{\text{hb}}(s\epsilon_{\text{HbO}_2}(\lambda) + (1-s)\epsilon_{\text{Hb}}(\lambda)) \ln(10)150\text{gL}^{-1}(64, 500\text{g mol}^{-1})^{-1}$ $\mu_s(a_{\text{mie}}, b, \lambda) = \frac{a_{\text{mie}}}{1-g} \left(\frac{\lambda}{500\text{nm}}\right)^{-b_{\text{mie}}}$							

simulation framework: GPU-MCML,²¹ 10^6 photons per simulation
 simulated samples: 550K
 sample wavelength range: 300-1000nm, stepsize 2nm

The approach by Preece is closest to the approach proposed in this manuscript. Unlike Preece et al, our approach does not need specific knowledge about the tissue composition, due to employing domain adaptation techniques to adapt the simulated data to real measurements. Furthermore, while Preece et al. work relied entirely on simulations, we also evaluate band selection in an *in vivo* context, ensuring that the simulations as well as the band selection results produce realistic estimates.

3. METHOD

The proposed method chooses bands that optimize a performance criterion with respect to a specific task (e.g. oxygenation monitoring) and domain (e.g. colonoscopy) without the need for annotated reference measurements. Core of the method is a generic simulated data set (Sect. 3.1). We investigate adaptation to the domain, using a novel domain adaptation technique (Sect. 3.2), followed by a selection of bands which minimize a task-specific criterion (Sect. 3.3) based on the adapted simulations. Figure 1 summarizes the proposed method.

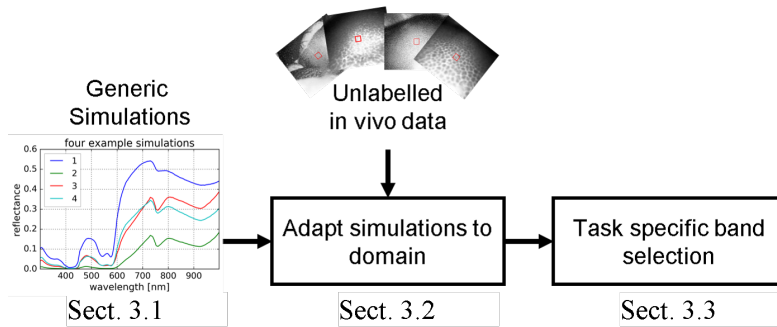


Figure 1: Overview of our approach. Generic simulations are adapted using unlabelled hyperspectral measurements from the target domain. The resulting domain-specific simulations are the basis for following task-specific selection of bands.

3.1 Reference data generation

Generic data is generated as described in,¹⁹ briefly revisited here. Tissue is assumed to be composed of three infinitely wide slabs. Each of these slabs are defined by values of blood volume fraction v_{hb} , reduced scattering coefficient at 500nm a_{mie} , scattering power b_{mie} , anisotropy g , refractive index n and layer thickness d . Using values for hemoglobin extinction coefficients ϵ_{Hb} and ϵ_{HbO_2} from literature, absorption and scattering coefficients μ_a and μ_s are determined for use in the MC simulation framework as described in.²⁰ A Graphics Processing Unit (GPU) accelerated version²¹ of the popular Monte Carlo Multi-Layered (MCML) simulation framework²² was chosen to generate spectral reflectances. The ranges from which the parameters are drawn and general simulation parameters are summarized in Table 2.

The wavelength range λ is large enough for adapting the simulations to cameras operating in the visible and near infrared. The spectral reflectances $r(\lambda)$ calculated by the MC simulation are transformed to the reflectance

measurement x_i at band i of the camera by:

$$x_i = \frac{\int_{\lambda_{\min}}^{\lambda_{\max}} o(\lambda)l(\lambda)f_i(\lambda)r(\lambda) d\lambda}{\int_{\lambda_{\min}}^{\lambda_{\max}} o(\lambda)l(\lambda)f_i(\lambda) d\lambda} \quad (1)$$

Here, $f_i(\lambda)$ characterizes the i th filter response, $l(\lambda)$ represents the relative irradiance of the light source and $o(\lambda)$ describes other parameters of the optical system like camera quantum efficiency or transmission of the optical elements. The camera reflectances are stained by multiplicative Gaussian noise to account for camera noise and inaccuracies arising from modelling tissue as homogeneous, layered structures.

3.2 Adapting to the target domain

The model from Sect. 3.1 describes a generic tissue, which shall encompass virtually all tissues with hemoglobin as main absorber. However, for a given domain such as cancer detection, many of the generated simulations might be irrelevant and thus bands selected to fit these simulations might be suboptimal. Domain adaptation techniques can ensure that the simulations match the target domain more closely.²³ In this manuscript, kernel mean matching (KMM),²⁴ a state-of-the-art domain adaptation technique, is used to automatically assign a weight to the simulations according to how closely they mimick real measurements taken from the target domain. More specifically, the following equation is minimized:

$$\arg \min_{\beta} \left\| \frac{1}{n} \sum_{i=1}^n \beta_i \phi(\mathbf{x}_i) - \frac{1}{n'} \sum_{i=1}^{n'} \phi(\mathbf{x}'_i) \right\|^2, \text{ s.t. } \beta_i \in [0, B] \text{ and } \left| \sum_{i=1}^n \beta_i - n \right| \leq n \frac{B}{\sqrt{n}} \quad (2)$$

This objective function matches the empirical means of simulations \mathbf{x}_i and real data \mathbf{x}'_i in a reproducing Kernel Hilbert Space induced by the function $\phi(\mathbf{x}_i)$. We set this function to the radial basis function kernel: $\phi(\mathbf{x}_i) = e^{-\gamma(\mathbf{x}-\mathbf{x}_i)^2}$.^{*} The first boundary condition limits the maximum influence of individual training samples, the second condition ensures $\frac{1}{n} \sum_{i=1}^n \beta_i \phi(\mathbf{x}_i)$ is close to a probability distribution.²⁵ Equation 2 cannot be minimized directly due to the possible infinite dimension of ϕ . The random kitchen sinks method²⁶ finds an approximate representation of $\phi(\mathbf{x}_i) \approx z(\mathbf{x}_i)$ by sampling from the Fourier transformation of a shift invariant kernel. This enables solving the convex KMM objective function in its non-kernelized form using a standard optimizer. The weights β_i are used to sample with replacing from the original data set to establish a data set which more closely resembles the real tissue.

3.3 Task-specific band selection

The band selection aims at selecting a subset of bands which retain as much of the capability to perform the chosen task as possible. If not mentioned otherwise, the chosen task is oxygenation estimation and the metric employed is mean absolute error (MAE) on the simulations. To compute the mapping from the reflectance to the oxygenation, the random forest regression method from²⁷ is employed. The method uses simulations to learn this mapping and was found to be more accurate than the conventional linear Beer-Lambert approaches. In principle, our method is compatible with any feature selection[†] or regression method. In this paper, we explore and compare the results of several popular filter as well as wrapper based approaches.

In a supervised setting, such as it is the case in this manuscript, filter methods typically estimate the quality of a feature set by computing mutual information and conditional mutual information scores between the features and the target variable as a proxy measure; wrapper methods evaluate the sets directly by using them in a machine learning algorithm. Since feature selection is an NP-hard problem, greedy step-wise optimization algorithms are often used to restrict the search space that is explored with both filter and wrapper methods.^{28,29}

^{*}Intuitively speaking, each simulation and measurement represents the center of a small Gaussian in reflectance space. Summed up, simulations and measurements respectively form distributions in reflectance space, made up from these Gaussians. The target of KMM is to re-weight the simulation Gaussians to reproduce the distribution of the measurements as closely as possible.

[†]Note that for the sake of consistency with the feature selection literature, we use the term feature rather than band in this section, but they are equivalent in the context of this work.

We used sequential forward selection (SFS) and best first search (BFS)²⁸ as wrapper feature selection methods. Both methods construct feature sets sequentially by greedily optimizing a fitness criterion for the explored feature sets. SFS simply explores adding single features to a given set. In each iteration, the feature that improves the fitness criterion the most is retained. We repeat this process until the criterion has not improved in the last three additions. BFS does not only explore adding but also removing features from an existing set and widens the search space by keeping track of all explored sets. If stuck in a local minimum, best first search falls back to previously explored well scoring feature sets and continues the search from there. Wrapper methods are flexible in the sense that one can use any fitness function to be optimized. We use the mean average error as shown in equation 3. A random forest regressor with parameters as proposed in²⁷ is used for all experiments.

$$\arg \min_{s_i \subset S} (l_{\text{MAE}}(y, f(x_{s_i}))) \quad (3)$$

S here denotes all features, s_i is the selected feature set (a subset of S), $l_{\text{MAE}}(y_i, f(x_{s_i}))$ is the mean average error achieved with set s_i , features x and regressor f for the target variable y (e.g. oxygenation). The cardinality of the feature set is given by $|s_i|$. $l_{\text{MAE}}(y_i, f(x_{s_i}))$ is computed by running a three fold cross-validation on the training set with the currently selected features. Final feature sets (and thus feature set size) are selected by evaluating the obtained sets on a test set.

For filter feature selection we used several commonly used mutual information-based selection criteria: Minimum Redundancy Maximum Relevance (mRMR),³⁰ Conditional Mutual Information Maximization (CMIM),³¹ Mutual Information based Feature Selection (MIFS),³² Interaction Capping (ICAP),³³ Conditional Infomax Feature Extraction (CIFE)³⁴ and Joint Mutual Information (JMI).³⁵ Brown et al.²⁹ provide a thorough analysis of these criteria and identify a unifying theoretical framework from which they can be derived. Although these methods were originally developed for classification problems, they can be used in the context of regression as well provided that a suitable mutual information estimator is chosen. This estimator must be able to compute the conditional mutual information $\text{MI}(x_i, x_j | y)$ if y is not categorical (where x_i and x_j are two feature vectors and y is the target variable). We use Kraskov’s nearest neighbor mutual information estimator for this purpose.³⁶ We optimize the feature sets by constructing them in a greedy step-wise manner as described in.²⁹ Filter feature selection returns the order with which features are added to the set but is incapable of returning the optimal number of features to be used. The number of features to be selected is therefore determined by evaluating sets of different sizes on the test set with the same random forest regressor as above.

Distance and angle to the tissue introduce multiplicative changes on the measured spectrum. To remove dependency on these factors, which cannot be controlled during an intervention, we perform band normalization. We follow recommendation of²⁷ and normalize each spectrum by its mean, followed by a $-\log$ transformation and a further l2 normalization. The $-\log$ and l2 is not necessary from a theoretical standpoint, put empirically improved results. Since our normalization method works on a per-sample basis and uses all the available bands for normalization, the data needs to be re-normalized whenever a different set of bands is used, also during feature selection. As a side-effect, this theoretically allows our approach to jointly optimize bands along with their normalization.

4. EXPERIMENTS AND RESULTS

Experiments were performed to assess the band selection results both in an *in silico* and *in vivo* setting. Sect. 4.1 describes the experimental setup with a specific focus on the parameters used to configure the algorithms. Purpose of the *in silico* experiments was to assess the method in a quantitative manner (Sect. 4.2). The *in vivo* experiments assessed how well oxygenation estimated from many bands can be reproduced by bands selected with the proposed method (Sect. 4.3).

4.1 Experimental setup

To validate our method, generic Monte Carlo reflectance simulations X_g were created from the model described in table 2. We split these generic simulations into two disjoint sets: a training (450,000 simulations) and a

test set (15,000 simulations). Bands were selected on a subset of 15,000 simulations from the training set. The selections were evaluated by training on the training set and evaluating on the test set.

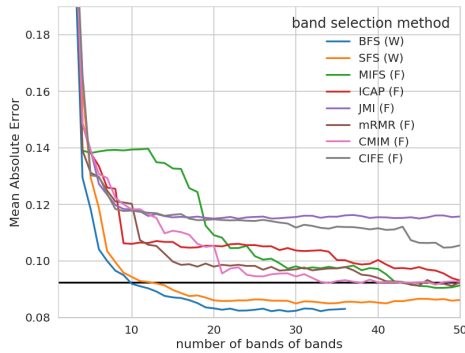
To mimic the camera used for the *in vivo* application, Equation 1 was used to simulate multispectral bands every 2nm from 500nm to 700nm with Gaussian band transmissions with a full width at half maximum (FWHM) of 20nm. Camera quantum efficiency and the optical system was assumed constant within the relatively narrow filter bands. Gaussian multiplicative noise (5%) emulated the camera noise. The range of 500nm to 700nm was chosen because the simulations and measurements (see sec. 4.2) did not match below 500nm and above 700nm. Further, when comparing the simulated data to the measurements, a 14nm shift in the absorption spectrum was detected. To align simulations and measurements, the measurements were shifted by 14nm. The *in vivo* measurements were transformed to reflectance by dark and flatfield correction. They were further blurred with a Gaussian kernel with a sigma of one pixel in the spatial domain to denoise the measurements.

Following the suggestions of Wirkert et al.,²⁷ the random forest was set to use ten trees, a maximum depth of nine and a minimum number of samples per leaf of ten. As in,¹⁹ the KMMs B parameter was set to ten and the kernel function's γ parameter was set to the median pairwise Euclidean sample distance determined on the training data.

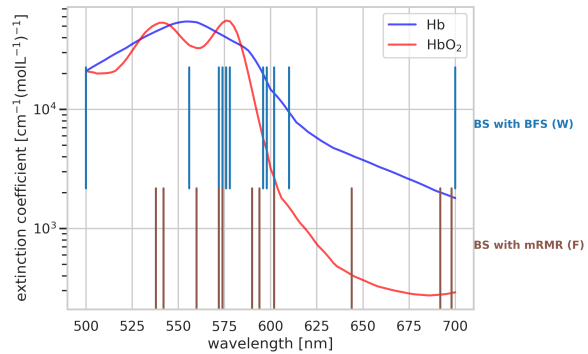
4.2 *In silico* validation

Purpose of the *in silico* experiments was to assess the different band selection techniques and the proposed domain adaptation approach in a quantitative manner.

Influence of band selection methods Several popular filter and wrapper methods were evaluated. Publicly available code for all feature selection methods used in this manuscript is provided at <https://github.com/FabianIsensee/FeatureSelection>. Results for these methods on the oxygenation task are shown in Figure 2a. The selected bands for the best filter and best wrapper method are shown in Figure 2b. Because wrapper methods performed better than filter methods and BFS is more powerful than SFS, BFS was selected as standard band selection technique for the following experiments.



(a) Comparison of different filter and wrapper methods



(b) Band selection results for selected methods

Figure 2: (a) Mean Absolute Error (MAE) of various band selection methods. Selected on the generic training set and evaluated on the test set. Wrapper methods (W) outperform filter methods (F). The black line is the result when training and testing on all 101 bands. (b) The first eleven selected bands from the best wrapper (BFS) and one of the best filter methods (mRMR) for the oxygenation estimation task. This number of bands was chosen as this is where BFS surpasses the baseline MAE achieved when using all bands.

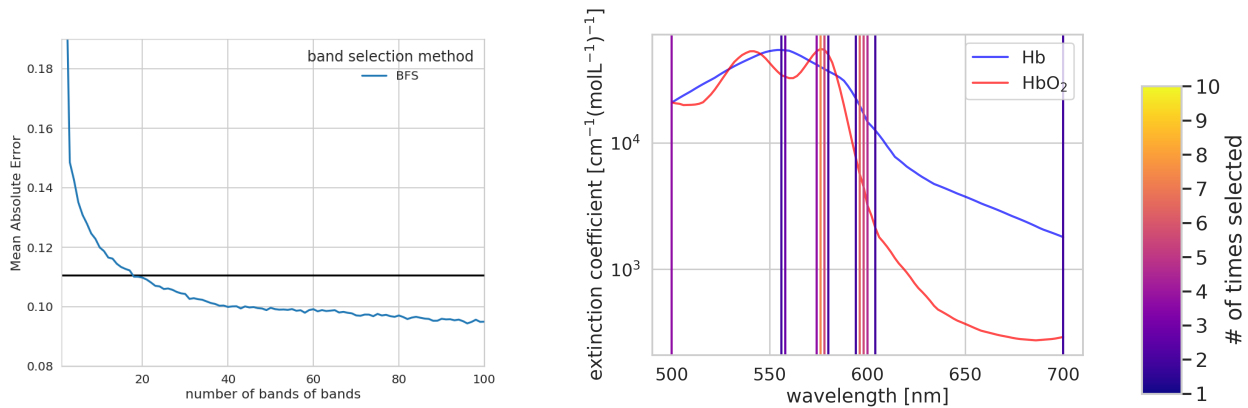


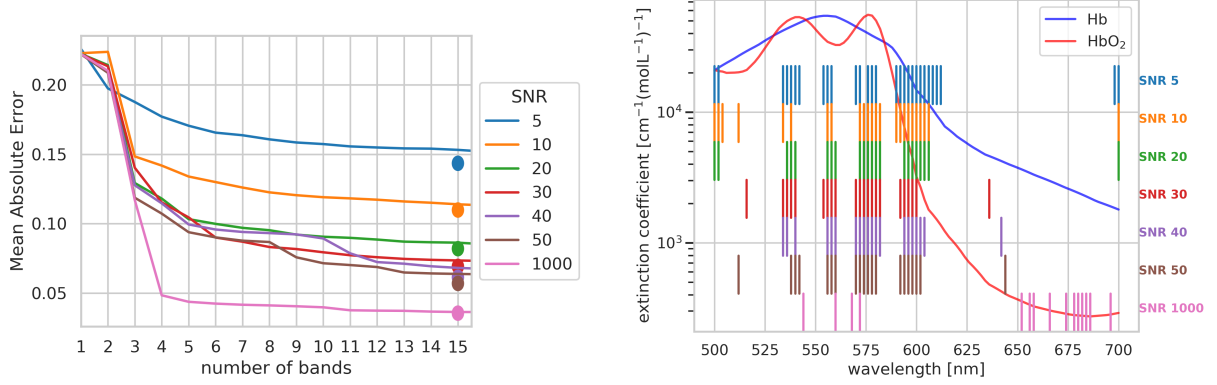
Figure 3: Redundant band experiment. To evaluate the tendency of BFS to select redundant bands, we create ten copies of each band, each with its own noise applied to it. This allows BFS to select a band more than once. Left: MAE achieved with an increasing number of selected bands (BFS). The horizontal line indicates the MAE achieved when using all 1010 bands. Right: The forty most relevant bands as selected by BFS in this experiment. The number of selections for each band is color coded.

Influence of redundant information on band selection results The band selection results from the last paragraph showed that BFS picked bands in close proximity (e.g. 578 and 576nm). This could suggest that there are few distinct places highly suited for oxygenation estimation and the algorithm tries to add redundancy by selecting nearby bands. To investigate this effect further we designed an experiment which gives the algorithm more freedom to build redundancy in the chosen bands. To this end, each band was duplicated ten times with differing random noise added (SNR=10). This corresponds to a maximum SNR of about 32 if all ten bands were selected. Figure 3 (right) shows the first 40 bands selected in this manner. The mean number of selections per band was 3.1. The highest number of selections were performed for center wavelengths of 576(7), 596(6) 598(5)nm and 578(5), where the number of selections is given in brackets.

Influence of noise on necessary number of bands This experiment should investigate how many bands are needed and whether or not this number of bands is dependent on the expected SNR of the multispectral system. The SNR in the simulations was varied between 5 (very high noise) and 1000 (virtually no noise). Note that unlike in the previous paragraph, bands are not duplicated and can be selected only once. Figure 4a shows how the SNR and number of selected bands influence the MAE. The circle shows the best result for each SNR. For noise levels of 5, 10, 20, 30, 40, 50, 1000 SNR, the minimum number of bands to be within a 0.001 margin of the best MAE for the SNR level was 29, 24, 22, 22, 20, 20 and 15 respectively. The *best MAE* hereby refers to the best band set identified throughout this experiment, not the 101 bands baseline. Figure 4b shows the selected bands.

Sources of noise, such as camera noise and model uncertainties, can be hard to quantify and known in advance. We therefore investigated the effect of selecting bands with one noise level and evaluating on another one. We chose the best set of fifteen bands with SNR levels of 5, 10, 20, 30, 40, 50 and 1000 because at this threshold SNR=1000 was within 0.01 of its best MAE. Evaluation was done using all combinations of bands and SNRs. Figure 5 shows how these factors interplay. As can be seen in the figure, bands selected at one noise level will not provide ideal results for another noise level. This is because high amount of noise favor the addition of neighboring and thus redundant bands earlier on in the band selection process to make the regressor more robust, while low amounts of noise allow for earlier stratification into other wavelength regions.

Influence of domain shift on band selection The influence of the target domain on the band selection and the possibility to adapt to the target domain using the method presented in Sect. 3.2 are investigated in



(a) Influence of noise level on MAE

(b) Influence of noise level on band selections

Figure 4: (a) Mean absolute error (MAE) on varying noise levels and number of selected bands. With 16 bands, performance for SNR=1000 is close to the best result indicated by the dot. (b) The stripes indicate the center wavelengths of bands for different noise levels. The number of bands shown here corresponds to the first combination to be within a margin of 0.01 compared to the best achieved mean absolute error (MAE). Hemoglobin extinction coefficients are plotted for reference.

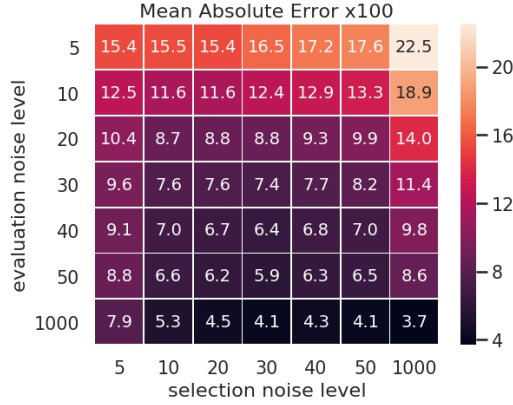


Figure 5: Performance when using different noise levels for selecting and applying bands. The matrix shows how the mean absolute error (MAE) varies when selecting fifteen bands on one noise level and training and testing these selected bands on another noise level.

the following. For this, a separate set of colon simulations X_c^\ddagger with 15,000 simulated reflectances drawn from the tissue model specified in Table 3 was created. 10,000 of these simulations were used to perform domain adaptation as described in Sect. 3.2 on X_g^{train} . The remaining 5000 simulations were used as a test set. To form a data set adapted to colonic tissue X_{ac} , 15,000 simulations were sampled with replacement using X_g^{train} and the weights determined by the domain adaptation.

Figure 6 shows how selection from domain adapted simulations compares to selection from unadapted data using BFS for band selection. For each experiment we indicate what data the bands were selected on (*BS on*) and what data was used for training the regressor (*tr on*). Evaluation was always done on the test set of the target domain X_c . We show results using general data X_g , domain adapted data X_{ac} and target domain data X_c (train) as source domain. Hereby, the results for X_g should be interpreted as a lower bound and the results for X_c are an upper bound. Note that in real-world scenarios data from the target domain is usually not available, rendering band selection on X_c impossible. As can be seen in Figure 6, domain adaptation can indeed close

[‡]As a reminder: X_g are generic simulations drawn from the parameters in table 2. X_c are colon tissue simulations drawn from the parameters in table 3. X_{ac} are simulations from X_g domain adapted to resemble X_c more closely

Table 3: Parameter ranges for the colon tissue model and their usage in the simulation set-up as described in.²⁷

	$v_{\text{hb}}[\%]$	$s[\%]$	$a_{\text{mie}}[\frac{1}{\text{cm}}]$	b_{mie}	g	n	$d[\text{mm}]$
layer 1 :	0-10	0-100	18.9 ± 10.2	1.289	.8-.95	1.36	.6-1.1
layer 2 :	0-10	0-100	18.9 ± 10.2	1.289	.8-.95	1.36	.4-.8
layer 3 :	0-10	0-100	18.9 ± 10.2	1.289	.8-.95	1.38	.4-.6

$$\mu_a(v_{\text{hb}}, s, \lambda) = v_{\text{hb}} (s \cdot \epsilon_{\text{HbO}_2}(\lambda) + (1 - s) \cdot \epsilon_{\text{Hb}}(\lambda)) \ln(10) 120\text{gL}^{-1} (64, 500\text{g mol}^{-1})^{-1}$$

$$\mu_s(a_{\text{mie}}, b, \lambda) = \frac{a_{\text{mie}}}{1-g} \left(\frac{\lambda}{500\text{nm}}\right)^{-b_{\text{mie}}}$$

simulation framework: GPU-MCML,²¹ 10^6 photons per simulation

simulated samples: 20K

sample wavelength range: 450-720nm, stepsize 2nm

the domain gap to some extent. While band selection did improve the MAE to below the respective baseline for X_g and X_c , this was not the case for X_{ac} . Across all number of selected bands, domain adaptation yielded better results than just using X_g . The light blue line shows the MAE when selecting on X_g but training on X_{ac} . This result indicates that, at least for the present data set, features may not need to be re-selected after domain adaptation.

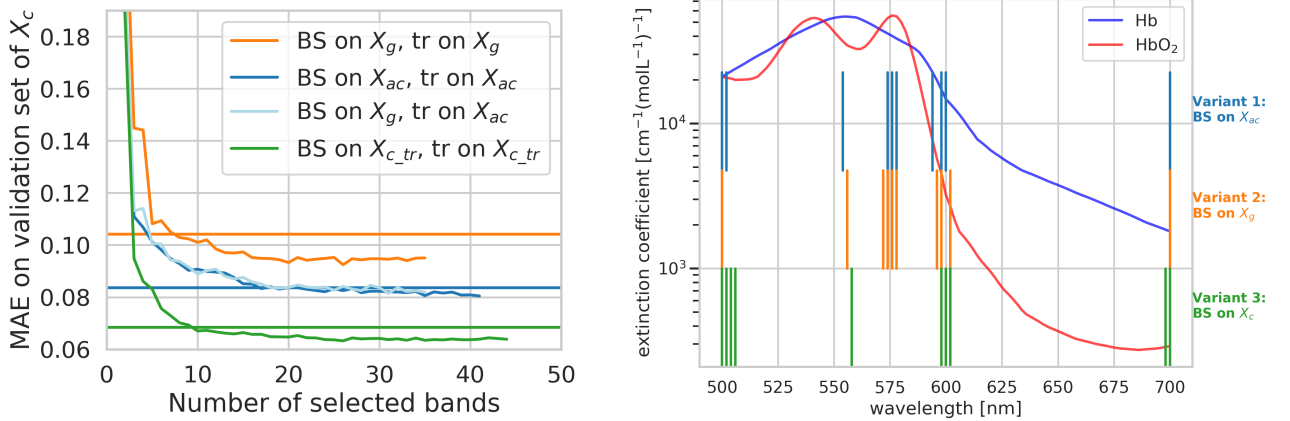


Figure 6: Left: Comparison of bands selections (BS) using domain aware X_{ac} (dark blue) and unadapted simulations X_g (orange). As an upper bound, the result of selecting on the simulated colon target domain X_c (green) is shown. The light blue line shows the result of training with bands selected on X_g but training with data from X_{ac} . All experiments were evaluated on the test set of the target domain (X_c). The horizontal lines are the results for training and testing on all 101 bands of the respective training set (no band selection). Right: The ten first bands selected for each of the different source domains.

4.3 In vivo validation

The *in vivo* validation investigates how well bands selected from the (domain adapted) simulations can reproduce oxygenation estimates on real data. Images from² were taken for this evaluation. They encompass eight hyperspectral images of head and neck tumors in a mouse model, captured by a Maestro (PerkinElmer Inc., Waltham, Massachusetts) imaging system. This system records hyperspectral images from 450-900nm with a FWHM of 20nm. Green fluorescence protein (GFP) fluorescence was used to identify tumorous tissue. For more details on the imaging process and the reference generation please refer to.² From the eight mouse tumor images, five were used for algorithm verification and three were reserved for the final validation of the band selection results. For the following analysis, bands between 500-700nm are considered, as only in these ranges a close match between simulations and measurements could be established. This relationship is analyzed in more detail in the next paragraph.

Matching simulations and real measurements We investigated how the simulations fit to the real mouse measurements for all pixels in the training images. For each of these measurements we determined the nearest neighbor from a set of 50,000 generic simulations from X_g , measured by the mean squared error (MSE). The median MSE was 66×10^{-4} . To get an intuition for these distances we plot exemplary fits in images 7h, 7i and 7j. To understand how the fit quality varies within an image, we report three of the training images, both as false RGB color image (recovered from hyperspectral measurements) and as fit error in Figure 7.

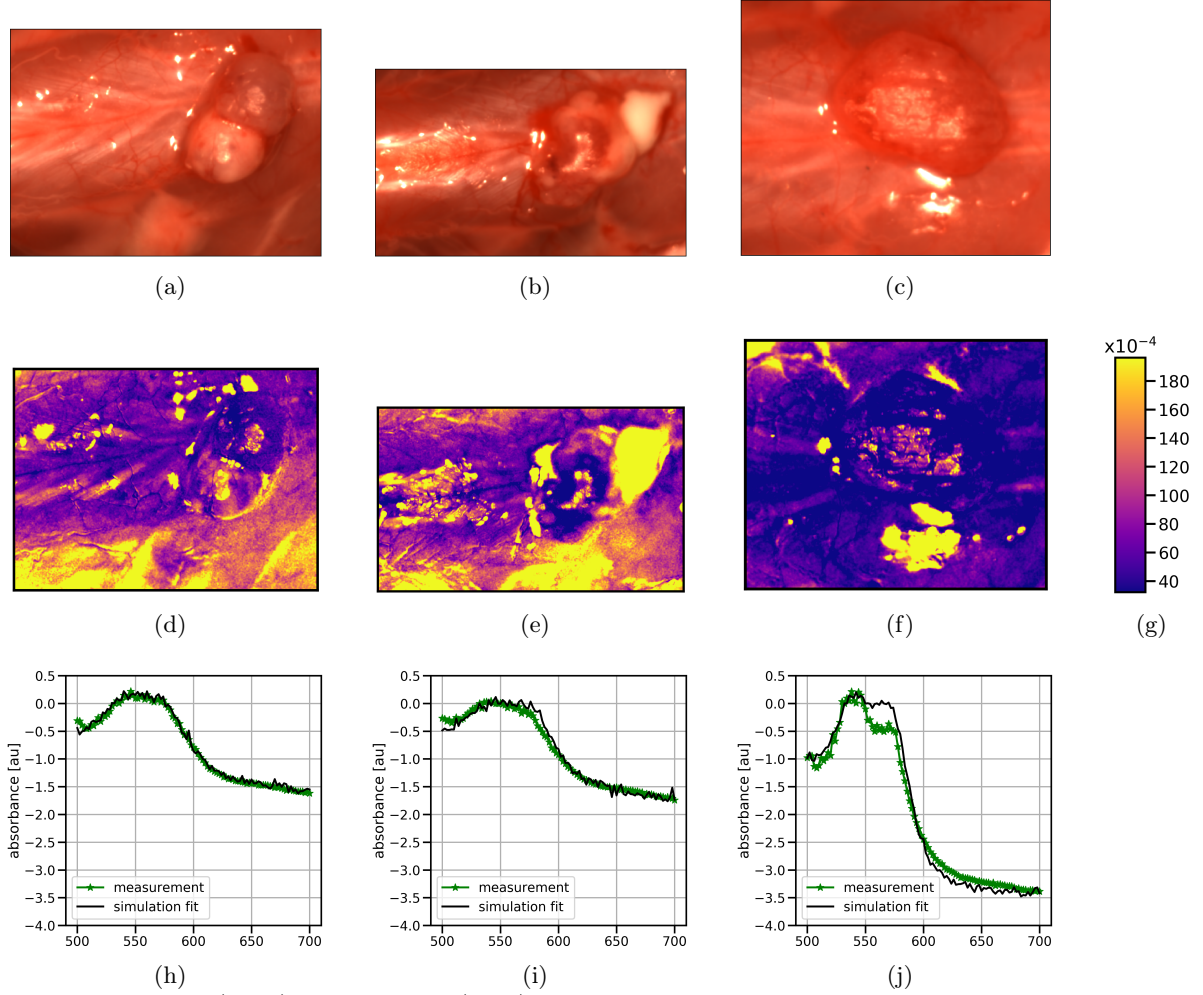


Figure 7: False RGB (a,b,c) and fit error (d,e,f) for three training images. The fit error for each pixel is the smallest mean squared error compared to data from X_g . (h,i,j) show the best simulation fit for the green points in the images above. They were selected to show a good (left), bad (middle) and very bad (right) fit.

Qualitative comparison of band selection methods The *in silico* methods evaluated the band selection in a quantitative, albeit simulated environment. In this experiment we compared selected methods in an *in vivo* setting. The guiding assumption was that the bands resulting from the band selection algorithms should be able to reproduce (and maybe improve upon) the full 101 band oxygenation estimate.

We focused on BFS, the best performing wrapper method. Experiments in this section are based on 15,000 measurements as a training set and another 15,000 measurements as a test set, sampled from X_g using weights from our domain adaptation approach. We select bands on the adapted training data, train a regressor on the training data with the selected bands and finally evaluate the regressor on the test set. The results for the band

selection on domain adapted *in silico* data are shown in Figure 8. As can be seen in the figure, the baseline MAE can be reproduced with 13 bands while the best MAE is achieved with 20 bands. Note that in this setup the band selection algorithm is agnostic to the real measurements as it is presented only domain adapted generic simulations. This approach allows us to select bands that are specific to some domain without having ground truth oxygenation values for the measurements.

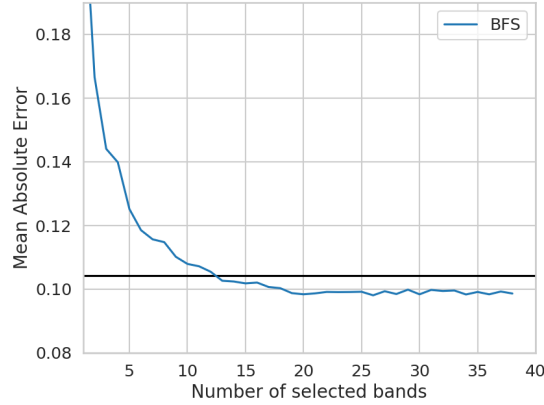


Figure 8: Band selection results on domain adapted data X_{am} for the *in vivo* experiment. Band selection was performed using BFS on the training set of X_{am} and the MAE are reported for the test set of X_{am} . Again, the horizontal line indicates the MAE achieved with all 101 bands. The best result was obtained with 20 bands. These bands are then used for the *in vivo* data. Note that the results displayed in this figure are based on domain adapted simulations only and do not provide a performance estimate for the *in vivo* data.

Final evaluation on test images In this final evaluation, we compare the BFS result using the 20 selected bands from the previous section with the 101 band oxygenation result. For this evaluation, three previously unused tumor images were used. See Figure 9 for a side by side comparison on the three images and violin plots of the tumor and non-tumor oxygenation results.

5. DISCUSSION

The contributions of this paper can be summarized as follows. Firstly, we are - to our knowledge - the first to investigate if a small subset of bands, selected using highly accurate simulations, can yield high-quality results on the clinically relevant task of oxygenation estimation. Secondly, we proposed the first method to select bands depending on a domain under investigation (here: head and neck tumor), without the need for often unavailable labeled *in vivo* data. The approach relies on selecting bands from a large generic database of labeled *in silico* reflectances generated with Monte Carlo methods. Recently proposed domain adaptation techniques were employed to select simulations which mimic the tissue of interest. Finally, we compared a large number of state-of-the-art band selection techniques as part of our framework. In the following, the results are discussed in light of the *in silico* and *in vivo* experiments.

***In silico* experiments** The *in silico* experiments investigated several aspects of the band selection algorithm in a controlled environment. The key findings were (a) wrapper outperform filter methods (b) ten bands give performance comparable to 101 bands in this setting (c) selecting more bands can yield better than baseline MAE in the case of wrapper methods (d) the algorithm adds redundant information by choosing neighboring bands (e) different noise levels impact band selection results with higher noise levels favoring redundancy early in the selection process (f) band selection is beneficial even when adding additional complexity to the experimental pipeline by incorporating the proposed domain adaptation technique.

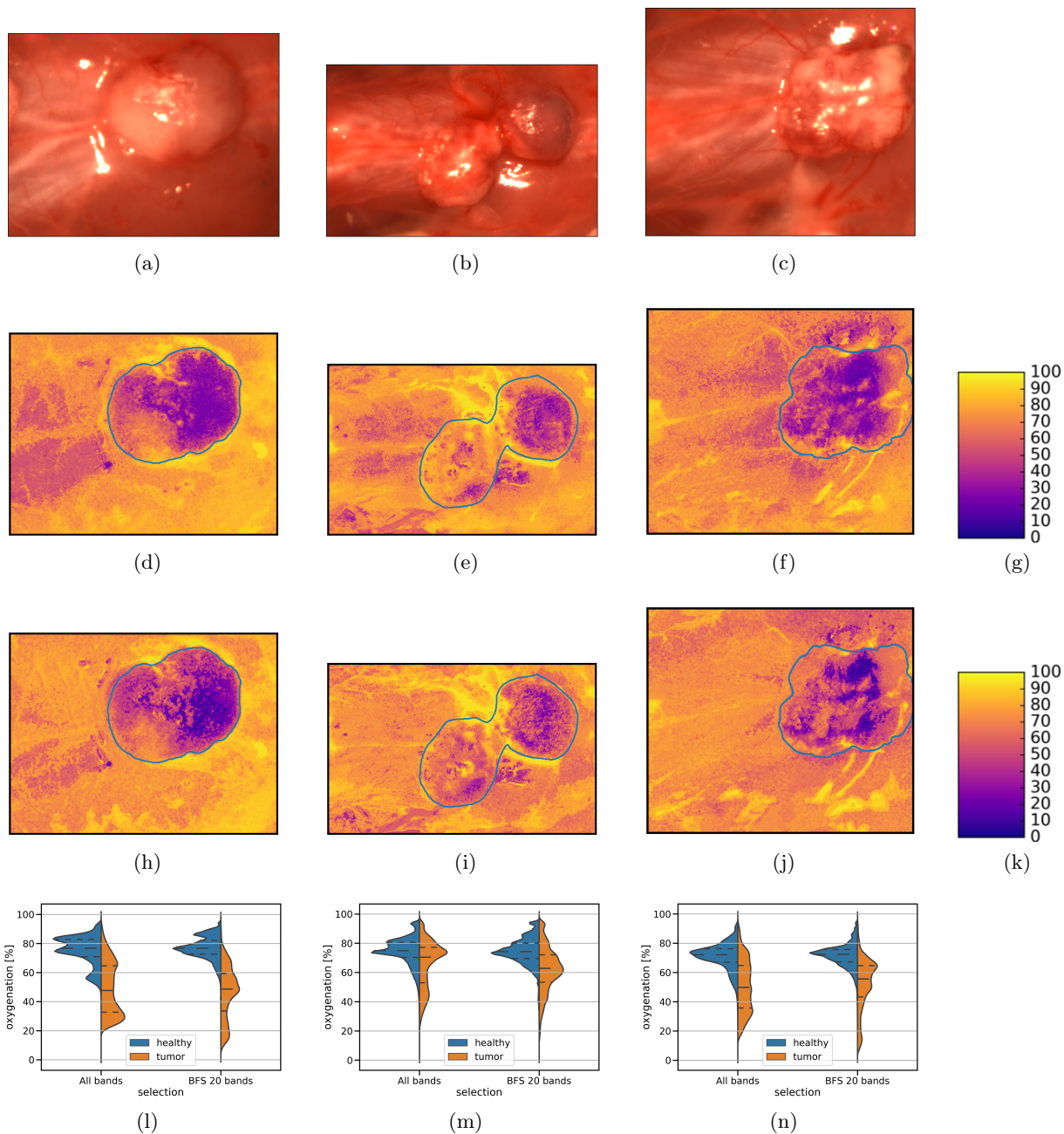


Figure 9: False RGB (a,b,c) of the final test tumor images. (d), (e), (f) show the oxygenation estimate using all 101 bands. (h), (i), (j) show the oxygenation estimate using only 20 bands selected with BFS. (l), (m), (n) show the violin plots, both for tumorous and benign regions. Tumorous regions were identified via GFP and are indicated by the blue outline in the images. (g) and (k) show the colorbar for the oxygenations in [%].

Wrapper methods consistently outperformed filter methods in our experiments. This is probably explained by being more “end-to-end” than the filter methods, which are agnostic to the downstream regression pipeline (here a random forest regressor). When looking at the selections specifically, it can be noticed that the filter methods select bands more broadly across the spectrum of possible wavelengths while wrappers first pick bands in places with high differences between oxygenated and deoxygenated hemoglobin while later adding redundancy

via neighboring bands. Adding redundant bands can be beneficial in the noise model used here (see below). This benefit could however not be captured by the heuristics employed in the filter methods. Filter methods typically penalize high mutual information between features in the selected set, thus pushing these methods away from selecting neighboring bands.

Our choice of normalization method is a design choice that needs to be discussed. In this work the band selection algorithms could influence the normalization because the nature of the normalization method used here required a re-normalization of the data whenever a feature was removed or added. To investigate the influence of the normalization method, we changed it to an image quotient norm³⁷ (data not shown). With the image quotient norm, this re-normalization step is unnecessary and therefore eliminates the possibility for the band selection algorithms to jointly optimize the regressor and the normalization. In our *in silico* experiments, image quotient norm therefore resulted in higher overall MAEs, the algorithms never surpassing the 101 band baseline and a less pronounced effect of the domain adaptation. Interestingly, in the *in vivo* experiments, image quotient normalization led to almost exact reproduction of the 101 band baseline result with 16 bands. A potential loss in MAE as observed in *in silico* is likely but could not be determined due to the lack of ground truth oxygenation. We leave a principled evaluation of the influence of normalization strategies to future work.

We further explored the benefits of redundancy by allowing the wrapper algorithms to select bands multiple times. Hereby, we could observe that only few very specific places are selected (see Fig. 3a). After a certain amount of bands the algorithm seems to focus on redundancy. This observation is in line with observations made by Guyon et al.³⁸ who report that redundant but noisy features are beneficial if used jointly to average out the noise. This behaviour is certainly linked to the independent multiplicative noise model applied to the simulated data and might change if the noise model would account for inter band dependencies. In our experiments using different SNR settings, it could be observed (Figure 4b) that, although the number of bands needed increases slightly when noise is added, the same general spectral areas seem to be selected (except for cases when very low noise levels are applied). Due to the varying noise levels, the wrapper method will sometimes start adding redundant bands sooner, sometimes later. Hereby, low noise levels favor more diverse regions within the spectral range because the robustness to noise via redundancy is not needed and the regressor can therefore fit the training data better. This results in sub-optimal feature sets when transferring them between different noise levels.

As expected, the chosen bands are mostly located close to areas of high difference in oxygenated and deoxygenated hemoglobin absorption. The bands selected by the algorithm are thus predominantly within a small spectral range of 530-610nm. A reason for this might be that spectra within this range are disturbed less by variation in other confounding factors such as scattering, which can be assumed constant within small ranges.

The domain shift experiment demonstrated the effectiveness of the domain adaptation technique used in this paper. Compared to training on the general simulation data, the domain gap could be closed partially (see horizontal lines in Figure 6). Using band selection in the context of a domain shift did not negatively impact results. Across all experiments done in this section, around 20 bands yielded the best oxygenation estimates. Interestingly, the selected bands are quite similar, especially between selection on X_g and X_{ac} . This is underlined by the light blue line in Figure 6 which shows that features selected on X_g are equally well suited as those selected on domain adapted data X_{ac} , indicating that feature sets selected on X_g may be broadly applicable across different domains.

The spectral range of the simulated camera was restricted to 500-700nm and the FWHM was set to 20nm. In future work, we will investigate how these results generalize to differing camera setups and normalization schemes. Embedded feature selection methods such as the one proposed in³⁹ could also be explored. Specifically, Cong et al. select features by adding a l1 regularization term to the loss function of a support vector machine (SVM). This naturally leads to a feature selection by driving weights of less important features down to 0. However, embedded approaches are considerably more restrictive compared to the wrapper methods employed here because they are limited to machine learning regressors that can incorporate such an additional regularization term.

***In vivo* experiments** The *in vivo* study relied on images of eight head and neck tumors in a mouse model. We investigated band selection of 101 bands ranging from 500-700nm. The key findings were (a) simulations and measurements show good alignment in this range, (b) experiments on data adapted to the target domain show

that BFS closely reproduces the MAE of the 101 band results for just 13 selected bands and achieved the best MAE with 20 bands (d) using these 20 selected bands for a qualitative analysis of the test images reveals similar predictions to the 101 bands estimate.

Interestingly, the contrast within the tumor regions seems to be sharper for the 20 bands selected by BFS. However, due to the lack of ground truth oxygenation data, quantitative evaluation of the band selection result is not possible for this experiment. Therefore, we are unable to definitively determine whether the MAE of the selected 20 bands is indeed lower than the 101 bands estimate, as suggested by our *in silico* experiments with domain adapted data (see Figure 8).

The simulated and measured spectra were shifted by 14nm and the spectral range with good coincidence was restricted to 500-700nm. One explanation for the shift is a mislabelling of the spectra in the measurement process, as the simulations were created using well-known absorption values for hemoglobin. A possible reason for the mismatch over 700nm might be the higher penetration depth of light for red/infrared wavelengths. This makes accurate simulation challenging because higher penetration depths also translates to more frequent occurrence of events that were not specifically modeled, which in turn results on variations in the spectra on real data that were not present in the simulations. A possible explanation for the mismatch below 500nm could be the GFP, which was injected to label the tumor.

An interesting finding not in focus of this work was that hypoxia seems to be detectable in tumors. If reproducible in future work this might be an important indication that multispectral imaging with a restricted set of bands can characterize important cancer hallmarks.

Conclusion We presented a method enabling task-specific band selection based on highly accurate simulations. *In vivo* and *in silico* results suggest the band selection can be performed purely *in silico*, which greatly increases flexibility and reduces costs for selecting appropriate bands.

ACKNOWLEDGMENTS

The authors would like to acknowledge support from the European Union through the ERC starting grant COMBIOSCOPY under the New Horizon Framework Programme under grant agreement ERC-2015-StG-37960. The research is further supported in part by NIH grants CA156775, CA204254, and HL140135.

REFERENCES

- [1] Lu, G. and Fei, B., “Medical hyperspectral imaging: a review,” *Journal of Biomedical Optics* **19**, 10901 (Jan. 2014).
- [2] Lu, G., Wang, D., Qin, X., Halig, L., Muller, S., Zhang, H., Chen, A., Pogue, B. W., Chen, Z. G., and Fei, B., “Framework for hyperspectral image processing and quantification for cancer detection during animal tumor surgery,” *Journal of Biomedical Optics* **20**(12), 126012–126012 (2015).
- [3] Sheffield, C., “Selecting Band Combinations from Multispectral Data,” in [*Photogrammetric Engineering and Remote Sensing*], (1985).
- [4] Beauchemin, M. and Fung, K. B., “On statistical band selection for image visualization,” *PE & RS- Photogrammetric Engineering and Remote Sensing* **67**(5), 571–574 (2001).
- [5] Guo, B., Gunn, S. R., Damper, R. I., and Nelson, J. D. B., “Band Selection for Hyperspectral Image Classification Using Mutual Information,” *IEEE Geoscience and Remote Sensing Letters* **3**(4), 522–526 (2006).
- [6] Chang, C.-I. and Wang, S., “Constrained band selection for hyperspectral imagery,” *IEEE Transactions on Geoscience and Remote Sensing* **44**, 1575–1585 (June 2006).
- [7] Sarhrouni, E., Hammouch, A., and Aboutajdine, D., “Dimensionality Reduction and Classification Feature Using Mutual Information Applied to Hyperspectral Images: A Wrapper Strategy Algorithm Based on Minimizing the Error Probability Using the Inequality of Fano,” *arXiv:1211.0055 [cs]* (Oct. 2012).
- [8] Du, Z., Jeong, M. K., and Kong, S. G., “Band Selection of Hyperspectral Images for Automatic Detection of Poultry Skin Tumors,” *IEEE Transactions on Automation Science and Engineering* **4**, 332–339 (July 2007).

- [9] Paul, A., Dey, A., Mukherjee, D. P., Sivaswamy, J., and Tourani, V., “Regenerative Random Forest with Automatic Feature Selection to Detect Mitosis in Histopathological Breast Cancer Images,” in [*Medical Image Computing and Computer-Assisted Intervention – MICCAI 2015*], Navab, N., Hornegger, J., Wells, W. M., and Frangi, A. F., eds., *Lecture Notes in Computer Science*, 94–102, Springer International Publishing (Oct. 2015).
- [10] Guyon, I. and Elisseeff, A., “An introduction to variable and feature selection,” *The Journal of Machine Learning Research* **3**, 1157–1182 (2003).
- [11] Wood, T. C., Thiemjarus, S., Koh, K. R., Elson, D. S., and Yang, G. Z., “Optimal feature selection applied to multispectral fluorescence imaging,” *Med Image Comput Comput Assist Interv* **11**(Pt 2), 222–229 (2008).
- [12] Han, Z., Zhang, A., Wang, X., Sun, Z., Wang, M. D., and Xie, T., “In vivo use of hyperspectral imaging to develop a noncontact endoscopic diagnosis support system for malignant colorectal tumors,” *Journal of Biomedical Optics* **21**(1), 016001–016001 (2016).
- [13] Nouri, D., Lucas, Y., and Treuillet, S., “Efficient tissue discrimination during surgical interventions using hyperspectral imaging,” in [*International Conference on Information Processing in Computer-Assisted Interventions*], 266–275, Springer (2014).
- [14] Nouri, D., Lucas, Y., and Treuillet, S., “Hyperspectral interventional imaging for enhanced tissue visualization and discrimination combining band selection methods,” *International Journal of Computer Assisted Radiology and Surgery* **11**, 2185–2197 (Dec. 2016).
- [15] Gu, X., Han, Z., Yao, L., Zhong, Y., Shi, Q., Fu, Y., Liu, C., Wang, X., and Xie, T., “Image enhancement based on *in vivo* hyperspectral gastroscopic images: a case study,” *Journal of Biomedical Optics* **21**, 101412 (May 2016).
- [16] Wirkert, S. J., Clancy, N. T., Stoyanov, D., Arya, S., Hanna, G. B., Schlemmer, H.-P., Sauer, P., Elson, D. S., and Maier-Hein, L., “Endoscopic Sheffield Index for Unsupervised In Vivo Spectral Band Selection,” in [*Computer-Assisted and Robotic Endoscopy*], Luo, X., Reichl, T., Mirota, D., and Soper, T., eds., **8899**, 110–120, Springer International Publishing, Cham (2014).
- [17] Marois, M., Jacques, S. L., and Paulsen, K. D., “Optimal wavelength selection for optical spectroscopy of hemoglobin and water within a simulated light-scattering tissue,” *Journal of biomedical optics* **23**(4), 041202 (2018).
- [18] Preece, S. J. and Claridge, E., “Spectral filter optimization for the recovery of parameters which describe human skin,” *IEEE Trans Pattern Anal Mach Intell* **26**, 913–922 (July 2004).
- [19] Wirkert, S. J., Vemuri, A. S., Kenngott, H. G., Moccia, S., Götz, M., Mayer, B. F. B., Maier-Hein, K. H., Elson, D. S., and Maier-Hein, L., “Physiological Parameter Estimation from Multispectral Images Unleashed,” in [*Medical Image Computing and Computer-Assisted Intervention - MICCAI 2017*], *Lecture Notes in Computer Science*, 134–141, Springer, Cham (Sept. 2017).
- [20] Jacques, S. L., “Optical properties of biological tissues: a review,” *Physics in Medicine and Biology* **58**, R37–R61 (June 2013).
- [21] Alerstam, E., Yip Lo, W. C., Han, T. D., Rose, J., Andersson-Engels, S., and Lilge, L., “Next-generation acceleration and code optimization for light transport in turbid media using GPUs,” *Biomedical Optics Express* **1**, 658–675 (Sept. 2010).
- [22] Wang, L. and Jacques, S. L., “Monte Carlo modeling of light transport in multi-layered tissues in standard C,” *The University of Texas, MD Anderson Cancer Center, Houston* (1992).
- [23] Pan, S. J. and Yang, Q., “A Survey on Transfer Learning,” *IEEE Transactions on Knowledge and Data Engineering* **22**, 1345–1359 (Oct. 2010).
- [24] Huang, J., Smola, A. J., Gretton, A., Borgwardt, K. M., Schölkopf, B., and others, “Correcting sample selection bias by unlabeled data,” *Advances in neural information processing systems* **19**, 601 (2007).
- [25] Gretton, A., Smola, A., Huang, J., Schmittfull, M., Borgwardt, K., and Schölkopf, B., “Covariate shift by kernel mean matching,” *Dataset shift in machine learning* **3**(4), 5 (2009).
- [26] Rahimi, A., Recht, B., and others, “Random Features for Large-Scale Kernel Machines,” in [*NIPS*], **3**, 5 (2007).

- [27] Wirkert, S. J., Kenngott, H., Mayer, B., Mietkowski, P., Wagner, M., Sauer, P., Clancy, N. T., Elson, D. S., and Maier-Hein, L., “Robust near real-time estimation of physiological parameters from megapixel multispectral images with inverse Monte Carlo and random forest regression,” *International Journal of Computer Assisted Radiology and Surgery* **11**, 909–917 (June 2016).
- [28] Kohavi, R. and John, G. H., “Wrappers for feature subset selection,” *Artificial intelligence* **97**(1-2), 273–324 (1997).
- [29] Brown, G., Pocock, A., Zhao, M.-J., and Luján, M., “Conditional likelihood maximisation: a unifying framework for information theoretic feature selection,” *Journal of machine learning research* **13**(Jan), 27–66 (2012).
- [30] Peng, H., Long, F., and Ding, C., “Feature selection based on mutual information criteria of max-dependency, max-relevance, and min-redundancy,” *IEEE Transactions on pattern analysis and machine intelligence* **27**(8), 1226–1238 (2005).
- [31] Fleuret, F., “Fast binary feature selection with conditional mutual information,” *Journal of Machine Learning Research* **5**(Nov), 1531–1555 (2004).
- [32] Battiti, R., “Using mutual information for selecting features in supervised neural net learning,” *IEEE Transactions on neural networks* **5**(4), 537–550 (1994).
- [33] Jakulin, A., *Machine learning based on attribute interactions*, PhD thesis, Univerza v Ljubljani (2005).
- [34] Lin, D. and Tang, X., “Conditional infomax learning: an integrated framework for feature extraction and fusion,” *Computer Vision–ECCV 2006*, 68–82 (2006).
- [35] Yang, H. H. and Moody, J., “Data visualization and feature selection: New algorithms for nongaussian data,” in [*Advances in Neural Information Processing Systems*], 687–693 (2000).
- [36] Kraskov, A., Stögbauer, H., and Grassberger, P., “Estimating mutual information,” *Physical review E* **69**(6), 066138 (2004).
- [37] Styles, I. B., Calcagni, A., Claridge, E., Orihuela-Espina, F., and Gibson, J. M., “Quantitative analysis of multi-spectral fundus images,” *Med Image Anal* **10**, 578–597 (Aug. 2006).
- [38] Guyon, I. and Elisseeff, A., “An introduction to variable and feature selection,” *Journal of machine learning research* **3**(Mar), 1157–1182 (2003).
- [39] Cong, Y., Wang, S., Liu, J., Cao, J., Yang, Y., and Luo, J., “Deep sparse feature selection for computer aided endoscopy diagnosis,” *Pattern Recognition* **48**, 907–917 (Mar. 2015).